LANGMUIR

pubs.acs.org/Langmuir Article

Discretized Motion of Surface Walker under a Nonuniform AC Magnetic Field

Yanjun Yang and Yiping Zhao*

Cite This: *Langmuir* 2020, 36, 11125−11137 Read Online

ACCESS | Metrics & More | Article Recommendations | Supporting Information

ABSTRACT: The motion of peanut-shaped magnetic microrods (PSMRs) with different magnetic moment (M_s) orientations φ_M under a nonuniform AC magnetic field has been investigated systematically. When gradually changing φ_M from 90° (perpendicular to the long axis of the PSMR) to 0°, the motion of the PSMR evolves from rolling to precession, then to tumbling. Systematic investigations on the translational velocity v_p versus the magnitude of the applied magnetic field B and the angular velocity ω_B show that the overall motion of the PSMRs can be divided into four different zones: Brownian motion zone, synchronized zone, asynchronized zone, and oscillation zone. The $v_p-\omega_B$ relationship can be rescaled by a critical frequency ω_c, which is determined by M_s, B, and a hydrodynamic term. An intrinsic quality factor q_m for the translational motion of a magnetically driven micro-/nanomotor is defined and is found to range from 0.73 to 13.65 T^{-1} in the literature, while the Fe PSMRs in the current work give the highest q_m (= 25.48 T^{-1}). High speed movies reveal that both the tumbling and precession motions of the PSMRs have a discretized nature. At the instances when the magnetic field changes direction, the PSMR performs an instantaneous rotation and the strong hydrodynamic wall effect would impose a driving force to move the PSMR translationally, and about more than 60% of the time, the PSMR neither rotates nor moves translationally. Based on this discretized motion nature, an analytic expression for q_m is found to be determined by the shape of the surface walker, the hydrodynamics near a wall, and the magnetic properties of the surface walker. This work can help us to better understand the motion of magnetic surface walkers and gain insight into designing better micro-/nanomotors.

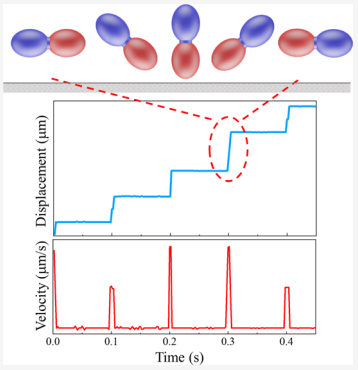

INTRODUCTION

Recently, magnetically controlled micro-/nanomotors have been found in an array of applications, such as cell manipulation,[1−3] cargo and molecular delivery,[4−6] disease treatment,[7−9] environmental remediation,[10] and so forth. Most of the applications require that the micro-/nanomotors should move translationally in the liquid, have a high controllability, and be easy to manipulate with a relatively fast translational velocity. There are two types of translational motion that a magnetically controlled micro-/nanomotor realizes, depending on its shape. One is the magnetic particle that can move freely inside a liquid. For example, a helical magnetic micro-/nanomotor can move translationally in a bulk fluid when it is rotating about its long helical axis.[11−15] The deformation of flexible magnetic particle chains can also induce translational motion in liquids.[16−18] The other one is a magnetic surface walker (MSW), which can only translate when the motor is very close to a surface (wall). The hydrodynamics between a magnetic particle and a wall introduces a driving force for the translational motion, and most translational motions of magnetic motors belong to this category.[19−22] The motion behavior of a MSW is rather complicated and depends on two important factors, the shape of the MSW and the applied magnetic field. The shape of the MSW can be categorized as a single particle,[23,24] a chain of particles,[25,26] and a cluster of particles.[21,27] Regardless of applied fields, most MSWs are anisotropic particles.

For the anisotropic MSWs, depending on the applied magnetic fields, several characteristic motion behaviors, such as rolling, tumbling, precession, and oscillating, are observed. For most MSWs, an out-of-plane rotating magnetic field (RMF) is applied.[1,19,28] In a recent study, premagnetized CoPt nanowires could perform the tumbling, precession, and rolling motions by changing the rotation frequency of an out-of-plane RMF.[29] If an in-plane RMF is applied, usually an anisotropic particle will perform a pure rotary motion with no translational motion.[30−32] Oscillating magnetic fields (OMFs) can also produce translational motion of a MSW. Huang et al. first reported translational motion of an anisotropic magnetic cluster under an OMF or a nonuniform AC magnetic field (nuAMF).[27] Later, Li et al. showed that a magnetic microdimer consisting of two Janus microspheres could roll

Received: July 20, 2020
Revised: August 21, 2020
Published: August 21, 2020

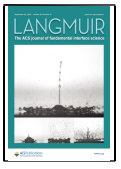

https://dx.doi.org/10.1021/acs.langmuir.0c02132
Langmuir 2020, 36, 11125−11137

back and forth on a surface under an OMF and attain a translational velocity up to 18.6 μm/s.[20]

A deeper investigation of literature reveals that the motion of a MSW not only depends on the applied field $\vec{B}$, but also on the orientation of the magnetic moment $\vec{M}_s$ of the MSW because the ultimate driving force for the translational motion is determined by the magnetic torque, $\vec{M}_s \times \vec{B}$. Take a rod-like MSW as an example (Figure S1). When the direction of the $\vec{M}_s$ is along the long axis of the rod, a tumbling motion is expected under an out-of-plane RMF (Figure S1A), a precession motion is predicted under a conical RMF (Figure S1E), and a spinning motion (Figure S1C) could be predicted under an in-plane RMF. For example, the magnetic microellipsoid was observed to perform spinning, precession, and tumbling motions under a RMF when the rotation axis of the RMF was changed from perpendicular to the substrate to parallel to the substrate, accompanied by an increased translational velocity.[32] When the $\vec{M}_s$ is perpendicular to the long axis of the rod, a rolling (Figure S1B) or precession (Figure S1F) motion is expected under a RMF. Based on classic mechanics, a tumbling motion with a large rotation radius should produce a faster translational velocity under the same rotation frequency. However, there is still no systematic study on how the orientation of $\vec{M}_s$ affects the motion of a MSW. One of the challenges is how to prepare MSWs with different $\vec{M}_s$ orientations while retaining the same shape and size.

In addition, although many MSWs have been reported, it is very hard to rigorously compare their motion performance so that suitable MSW design or motion conditions can be selected for different applications. In the micro-/nanomotor community, the velocity v_p to body length l ratio is usually used to characterize the performance of a translational motor. Gao et al. summarized the v_p/l ratio for many different micro-/nanomotors.[33] However, the v_p of a MSW is not only determined by its shape or dimension, but also by the applied magnetic field, especially the field frequency f_B. It has been observed experimentally that v_p increases monotonically with f_B until it reaches a maximum at a critical frequency, where the synchronized rotation of the MSW changes to an asynchronized one. Thus, the v_p/l ratio is not an intrinsic parameter for characterizing the translational motion of a MSW. Therefore, a different universal parameter is needed to uniquely characterize and compare the motion performance of the magnetic micro-/nanomotors, normalizing the effects from the driving field B and f_B.

Finally, in most MSW literatures, the motion of the MSW is always described by the continuum hydrodynamics with a constant resistant matrix. For example, when driven by an out-of-plane RMF, a rolling magnetic microsphere constantly experienced a driven torque induced by the friction, and the translational displacement increased almost linearly because, in an ideal case, the distance between the surface of the particle and the wall is a constant.[34] This idea was adapted by Yang et al. to predict the translational motion of the wheel-shaped magnetic cluster on topographic surfaces.[21] However, for an anisotropic particle, such a treatment is not valid. In fact, the numerical simulation from our previous publication[27] showed that the translational displacement of a tumbling magnetic spheroid was stepwise: the spheroid started to rotate and the hydrodynamic interaction between the rotated spheroid and the substrate induced a driving force to move the particle forward only when the magnetic field changed direction; but most times, the particle neither rotated nor moved forward.[27] If this discretized motion picture is used, then the governing equations for an anisotropic MSW would be very different, or piecewise. Therefore, another important question needs to be answered is whether or not the discretized motion is correct. If it is, how should we describe the motion of the MSW and compare the motion performance?

In this paper, we will target the above three important questions for the MSW. First, we demonstrate that by changing the reduction condition of the Fe_2O_3 PSMRs, PSMRs with different $\vec{M}_s$ orientations can be obtained. A systematic study on how the $\vec{M}_s$ orientation affects the motion of PSMRs is performed. Second, an intrinsic quality factor q_m for the motion of the PSMR is defined. By comparing the q_m in the literature and from our current work, we show that the tumbling motion of the Fe PSMR has achieved the best q_m. Finally, the fast CCD movies show that both the tumbling and precession motions of the PSMR are discretized, and the q_m is determined by the shape of the MSW, the hydrodynamics near a wall, and the magnetic property of the MSW.

EXPERIMENTAL SECTION

Materials. Iron chloride hexahydrate ($FeCl_3 \cdot 6H_2O$, 99%) was obtained from Acros Organics. Sodium hydroxide (NaOH, ≥97.0%), sodium sulfate (Na_2SO_4, ≥99.0%), and sodium dodecyl sulfate (SDS, ≥99.0%) were obtained from Sigma. All chemicals were of analytic grade and were used without further purification. Deionized water (DI water) was used for all experiments.

Fabrication of the Peanut-Shaped Magnetic Microrods. The peanut-shaped magnetic microrods were synthesized by a hydrothermal method according to a previous report.[35] Briefly, 27 mL of 6.0 M NaOH was slowly added into 30 mL of 2.0 M $FeCl_3$ in an autoclave for 30 min with continuous stirring, followed by the addition of 3 mL of 0.75 M Na_2SO_4 solution. The mixture was agitated for an additional 10 min. Then, the autoclave was transferred into an oven preheated to 100 °C and maintained for 8 days. The resulting suspension was washed 5 times with DI water and magnetically separated to remove unreacted chemicals. The as-synthesized PSMRs (we refer as Fe_2O_3 PSMRs) were then resuspended in a 20 mM SDS solution to obtain a concentration of 5.8×10^7 particles/mL for further experiments.

Reduction of Fe_2O_3 PSMRs. The overnight dried Fe_2O_3 PSMRs in a ceramic boat were placed in the furnace (Lindberg/Blue M Company) and annealed in N_2 (50 sccm) carried ethanol flow at 350 °C for 2, 4, and 6 h, respectively. We refer to the 6 h reduction sample as Fe PSMRs. The reduced PSMRs were then resuspended in an SDS solution (20 mM) to obtain a concentration of 5.8×10^7 particles/mL for further experiments.

Magnetization of the PSMRs. Both 1.5 mL of Fe_2O_3 PSMR and Fe PSMR suspensions were placed in a constant magnetic field of 1.5 T generated by two solenoids for 10 min to magnetize the PSMRs so that in the motion experiments, the magnetic moment of the PSMRs can be treated as a constant.

Characterizations of the PSMRs. The morphologies of the PSMRs were obtained by a field emission scanning electron microscope (S-4800, Hitachi, Japan) operating at 5 kV. The crystal structures of the dried PSMRs on a glass slide were characterized by a PANalytical X'Pert PRO MRD X-ray diffractometer (XRD, Malvern Panalytical, England) with a fixed incidence angle of 0.5°. The XRD scans were recorded with a Cu Kα_1 radiation (λ = 1.541 Å) in the 2θ range from 15 to 80° with a step size of 0.030°. The Raman measurements were performed by a confocal Raman microscope (InVia, Renishaw, England) using a 785 nm excitation laser (9 mW at sample), 20× objective lens, and 10 s acquisition time. The magnetic property measurements of the dried PSMRs were carried out by a vibrating sample magnetometer (model EZ7, MicroSense, USA) over a magnetization field range from −15,000 to 15,000 Oe.

https://dx.doi.org/10.1021/acs.langmuir.0c02132
Langmuir 2020, 36, 11125−11137

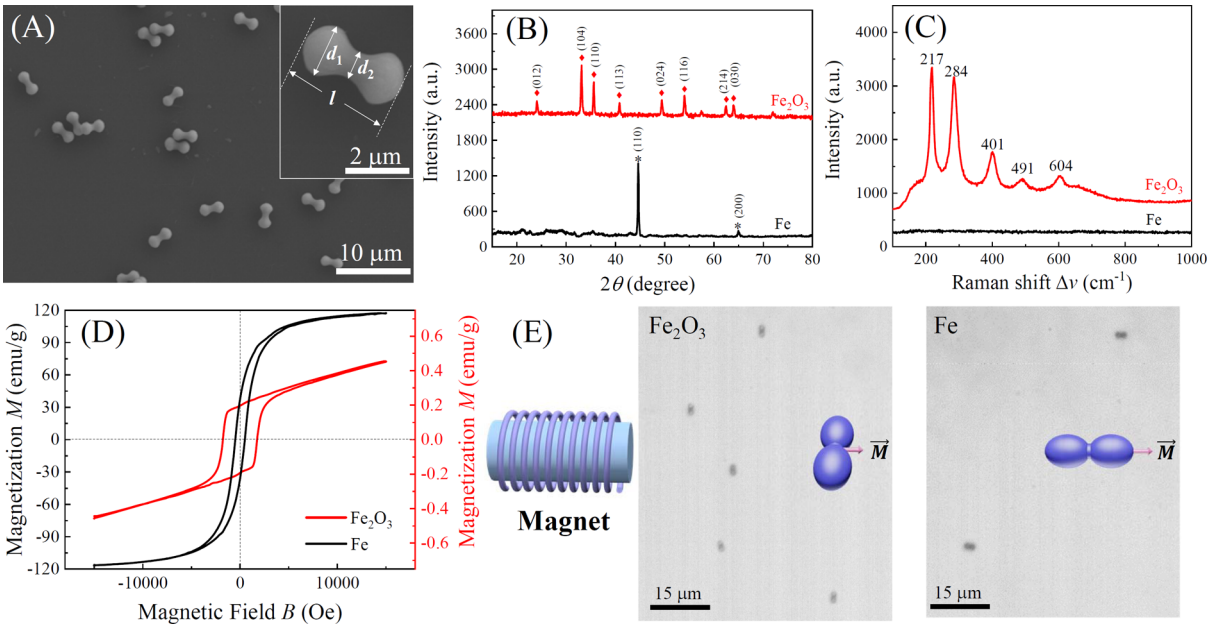

Figure 1. (A)Representative SEM image of Fe_2O_3 PSMRs. The (B) XRD patterns, (C) Raman spectra, and (D) magnetic hysteresis loops of Fe_2O_3 PSMRs and Fe PSMRs. (E) Magnetic moment orientation of Fe_2O_3 PSMRs and Fe PSMRs under a static magnetic field.

Motion Observation System. A single magnetic solenoid system has been used, similar to our previous report.[27] As shown in Figure S2 of the Supporting Information, the AC magnetic field for the PSMR motion was generated by a solenoid (Air-Core Solenoid#14825, Science Source, USA) with a cast iron core. The solenoid was connected to a 2-channel current supply (PLX3602, QSC, USA), and its input AC current with a frequency f_B (5−100 Hz) and a current amplitude I_0 (0.25−2.5 A) was programmed by a sound card in a computer using a homemade MATLAB program. The suspension of the PSMRs was carefully transported into a rectangular glass capillary tube (height: 0.1 mm and width: 2 mm, VitroCom). The capillary tube was placed in the magnetic system under a long-working distance optical microscope (FS110, Mitutoyo, Japan). The observation location was L = 27.2 mm away from the front face of the solenoid. The magnetic field at the observation location was measured and calibrated by a Gauss meter (5180, F.W.BELL, USA). All movies were obtained by a fast CCD camera (V9.1, Phantom, USA) through the microscope with a 50× objective lens. During the experiments, the camera recording speed was set to be 10, 50, and 100 times the frequency f_B. The obtained movies were analyzed using in-house cluster tracking MATLAB program.

RESULTS AND DISCUSSION

General Motion Behavior of PSMRs with Different Magnetic Moment Orientations. Figure 1A shows the representative morphology of the Fe_2O_3 PSMRs. They are dumbbell-shaped with a length l = 3.48 ± 0.06 μm in the long-axis, a large width d_1 = 1.70 ± 0.03 μm, and a small width d_2 = 1.00 ± 0.03 μm in the short axis as shown in the insert. The volume of each Fe_2O_3 PSMR was calculated to be around 5.03 μm^3 (see Section S3 in the Supporting Information). The XRD patterns of the Fe_2O_3 PSMRs and Fe PSMRs shown in Figure 1B indicate that the Fe_2O_3 PSMRs are the rhombohedral phase of α-Fe_2O_3 (hematite) [space group: $R\bar{3}c$ (JCPDS, no. 33-0664)], while the Fe PSMRs are the pure body-centered structure of Fe (JPCDS no. 06-0696). The Raman spectra shown in Figure 1C further confirm the results from XRD. For the Fe_2O_3 PSMRs, five Raman resonant peaks of α-Fe_2O_3, the two peaks at $\Delta\nu$ = 217 and 491 cm^{-1} attributed to the A_{1g} mode, and the three peaks at $\Delta\nu$ = 284, 401, and 604 cm^{-1} due to the E_g mode, are visible.[36] No Raman peaks are shown for Fe PSMRs because of the symmetry of the Fe crystal and selection rules for Raman. Both XRD patterns and Raman spectra indicate the high degree of conversion from α-Fe_2O_3 to Fe after the reduction. Because of the change of the material density, the morphology of the Fe PSMRs is estimated as l' = 3.26 μm, d_1' = 1.48 μm, and d_2' = 0.78 μm (see Section S4 in the Supporting Information). The magnetic hysteresis loops of the PSMRs are shown in the Figure 1D illustration. The Fe_2O_3 PSMRs have a residual magnetization $M_r^{Fe_2O_3}$ = 0.198 emu/g (i.e., the moment of a single Fe_2O_3 PSMR is $M_s^{Fe_2O_3}$ = 5.20 × 10^{-12} emu), and a coercivity of $H_c^{Fe_2O_3}$ = 1726 Oe. These values are very close to M_r (= 0.278 emu/g) and H_c (= 1560 Oe) of the bulk hematite;[37] while M_r^{Fe} = 38.64 emu/g (or M_s^{Fe} = 1.49 × 10^{-9} emu) and H_c^{Fe} = 490 Oe for Fe PSMRs, which is significantly different from the corresponding bulk values (M_r = 220.7 emu/g and H_c = 0.9 Oe).[38] These discrepancies could be due to the porous morphology of the Fe PSMR, or the conversion of Fe_2O_3 to Fe may not be completed in the reduction process.[39] The orientation of M_s is different as shown in Figure 1E when the suspensions of PSMRs were observed under a horizontally applied constant magnetic field B. For the Fe_2O_3 PSMRs, all of the particles were aligned with their long axes perpendicular to the applied magnetic field while for the Fe PSMRs, the magnetic moment direction of each particle is along the long axis. The magnetic moments of as-synthesized Fe_2O_3 PSMRs are determined by the crystal orientation and growth dynamics of the particle. Previous publication showed that during the growth of Fe_2O_3 PSMRs, the overall c-axis of the Fe_2O_3 crystal is along the long axis direction and the magnetic dipole moment direction is in the perpendicular or transverse direction.[40] The reduction of Fe_2O_3 PSMRs to Fe PSMRs is a high temperature process and can be considered under equilibrium, therefore the resulting magnetic moments would depend on the total magnetic energy of the particle. According to ref 41, an elongated Fe particle

https://dx.doi.org/10.1021/acs.langmuir.0c02132
Langmuir 2020, 36, 11125−11137

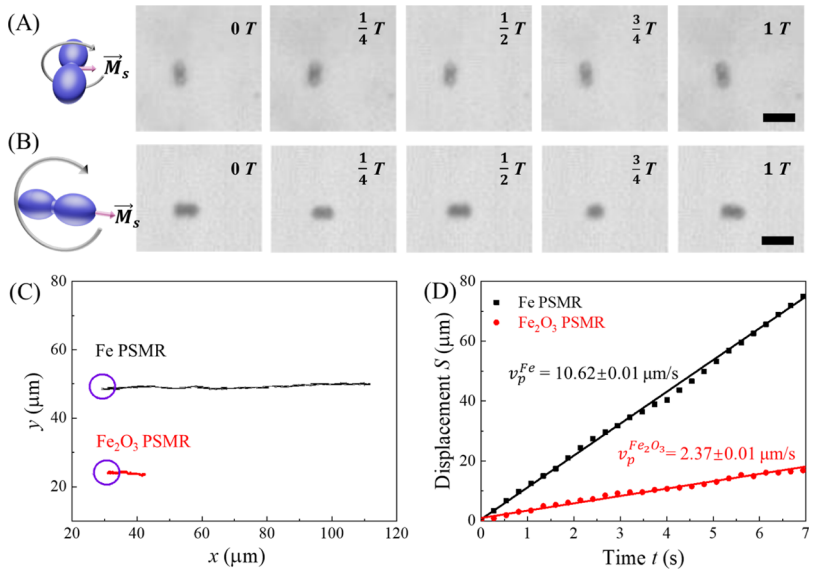

Figure 2. Cartoon and movie snapshots of (A) a rolling Fe_2O_3 PSMR and (B) a tumbling Fe PSMR within one period (T = 0.067s) under a nuAMF of B = 3.46 mT and f_B = 15 Hz. Scale bar: 5 μm. (C) Trajectory and (D) displacement S vs time t plots of a Fe_2O_3 PSMR and a Fe PSMR. The slope from the linear fitting (solid line) in (D) gives the corresponding translational velocity v_p.

minimizes its shape energy by aligning its magnetization direction with the long axis of the particle.

The motion of both the Fe_2O_3 PSMRs and Fe PSMRs was observed under a nuAMF at different applied field magnitudes B and frequencies f_B. To ensure the consistency of the experiments, all of the PSMR suspensions were magnetized at a constant magnetic field of 1.5 T prior to the motion experiments. Figure 2A,B shows time-lapse optical microscopy images of a Fe_2O_3 PSMR and a Fe PSMR under a nuAMF with B = 3.46 mT and f_B = 15 Hz (i.e., the period T = 0.067 s) (the corresponding movies are Movies M1 and M2 in the Supporting Information). Regardless the type of PSMR, the PSMR was moving almost horizontally away from the solenoid (the solenoid was place on the left in Figure 2A,B) as shown in the trajectories of Figure 2C. These results are consistent with our previous report.[27] However, during the motion for the Fe_2O_3 PSMR as shown in Figure 2A, the long axis of the PSMR was always perpendicular to the applied magnetic field direction and the PSMR would roll about the long axis as shown in Movie M1 (in-plane rolling). More detailed movie analysis shows that during the rolling of the Fe_2O_3 PSMR, its long axis vibrated back and forth. Thus, the Fe_2O_3 PSMR exhibited a slight precession motion[29,42] about the vertical direction, with a very small precession angle φ_p = 7.4 ± 0.2 (see Section S5 and Figure S6B in the Supporting Information). This precession angle φ_p is independent of B and f_B (Figure S6C). For the Fe PSMR shown in Figure 2B and Movie M3, the PSMR flipped out-of-plane rapidly (out-of-plane rolling), that is, the tumbling motion. The comparison of the trajectories of the two PSMRs are shown in Figure 2C, within the same time period (t = 7 s). The Fe PSMR traveled a much longer distance than that of the Fe_2O_3 PSMR. Figure 2D shows the plots of the displacement S of the two PSMRs versus time t. Both $S-t$ plots show a linear relationship with very different slopes: for the Fe_2O_3 PSMR, the slope gives a translational velocity $v_p^{Fe_2O_3}$ = 2.37 μm/s, while for the Fe PSMR, v_p^{Fe} = 10.62 μm/s, that is, the velocity of the Fe PSMR is almost 5 times the speed of the Fe_2O_3 PSMR under the same external magnetic field and applied frequency conditions. This ratio is significantly larger than the aspect ratio γ (= l/d = 2–3.5) of the PSMR. It appears that the translational speed is directly related to the rotation radius of the PSMR. In a previous report, an Fe_2O_3 PSMR with $l \sim 3$ μm and $d_1 \sim 1$ μm could only reach a translational speed of 1.23 μm/s with a rolling motion under an out-of-plane RMF with f_B = 15 Hz and B = 3.6 mT, while under a conical RMF with f_B = 15 Hz and B = 3.6 mT, its speed became 2.72 μm/s,[1] which is slightly larger than the speed obtained for our Fe_2O_3 PSMR under a nuAMF with similar conditions.

The origin of the nuAMF-induced translational motion of PSMR has been discussed in detail in our previous publication.[27] Under a low Reynolds number condition [the maximum Reynolds number (= $\rho v_p l/\eta$, where ρ and η are the density and viscosity of the liquid, respectively)] is calculated to be less than 10^{-3} based on the velocity of the Fe PSMR), if a PSMR is rotating near a wall, the wall will break the rotational symmetry and induce translational motion. Initially, a small magnetophoresis force (due to the field gradient generated by the nuAMF) would introduce a torque to make the PSMR rotate clockwise (if the solenoid is placed at the left of the PSMR) because of the hydrodynamic pressure difference between the two ends of the PSMR. Then, the applied alternating AC magnetic field would sustain the rotation, and the interaction of the PSMR and the wall would induce a driving force (friction) to move the PSMR translationally.

If the slight precession angle for the motion of the Fe_2O_3 PSMR can be neglected, then regardless of the orientation of the magnetization of the PSMR, the linear translational motion is induced by the rolling of the PSMR on top of a substrate surface. The translationally driven force is induced by the magnetic torque $\tau_M = M_s B \sin \omega_B t \sin \beta$ where the external magnetic field $B \sin \omega_B t$ ($\omega_B = 2\pi f_B$) is applied along the x-axis and β is the angle between the magnetic moment $\vec{M}_s$ and the x-axis (see Figure 3). According to Yang et al. and under the low Reynolds number approximation,[34] a general free body diagram for these two cases can be sketched (Figure 3A for the Fe_2O_3 PSMR and Figure 3B for the Fe PSMR), and the equations of motion for a PSMR are given by

https://dx.doi.org/10.1021/acs.langmuir.0c02132
Langmuir 2020, 36, 11125−11137

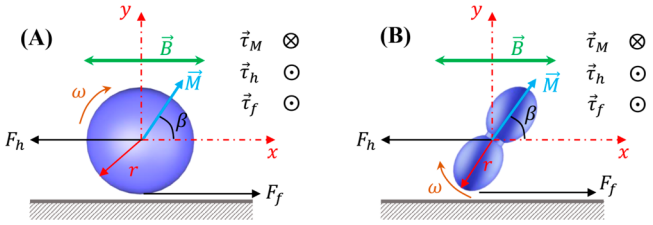

Figure 3. The free body diagram for (A) a rolling Fe_2O_3 PSMR and (B) a tumbling Fe PSMR near the substrate.

$$\sum F_x = F_f - F_h = 0 \tag{1}$$

$$\sum \tau = -\tau_M + \tau_h + rF_f = 0 \tag{2}$$

where F_f is the friction between the PSMR and the substrate, F_h is the hydrodynamic drag force due to rotation and translation, τ_h is the hydrodynamic torque, and rF_f is the torque induced by friction. When the PSMR is close to the substrate, the apparent viscosity of the portion facing the substrate surface is increased. The PSMR experiences a friction force F_f due to the interaction between the PSMR and the substrate to induce the translational speed. It is also reasonable to assume that v_p is proportional to $r\omega_p$, the speed of the rotating object at the contact point (r is the radius of the PSMR ($r = d_1/2$ for the Fe_2O_3 PSMR and $r = l/2$ for the Fe PSMR), and ω_p is the angular speed of the PSMR),[34] and their ratio

$$\xi = \frac{v_p}{r\omega_p} \tag{3}$$

is called the slipping coefficient, which can be used to characterize a translational motion due to rotation. The ξ depends on the complicated rotation geometry and hydrodynamic interaction of the system (see Section S6 of the Supporting Information). The hydrodynamic interaction, $\vec{F}_h$ and torque $\vec{\tau}_h$, can be related to its locomotion with a resistance matrix $M_h = \begin{bmatrix} a & b \\ c & d \end{bmatrix}$ (here, we only consider a single rotation axis so that M_h is simplified)[43]

$$\begin{pmatrix} F_h \\ \tau_h \end{pmatrix} = \begin{bmatrix} a & b \\ c & d \end{bmatrix} \begin{pmatrix} v_p \\ \omega_p \end{pmatrix} \tag{4}$$

where a, b, c, and d are the hydrodynamic drag coefficients of the PSMR near a wall and their expression depends on the

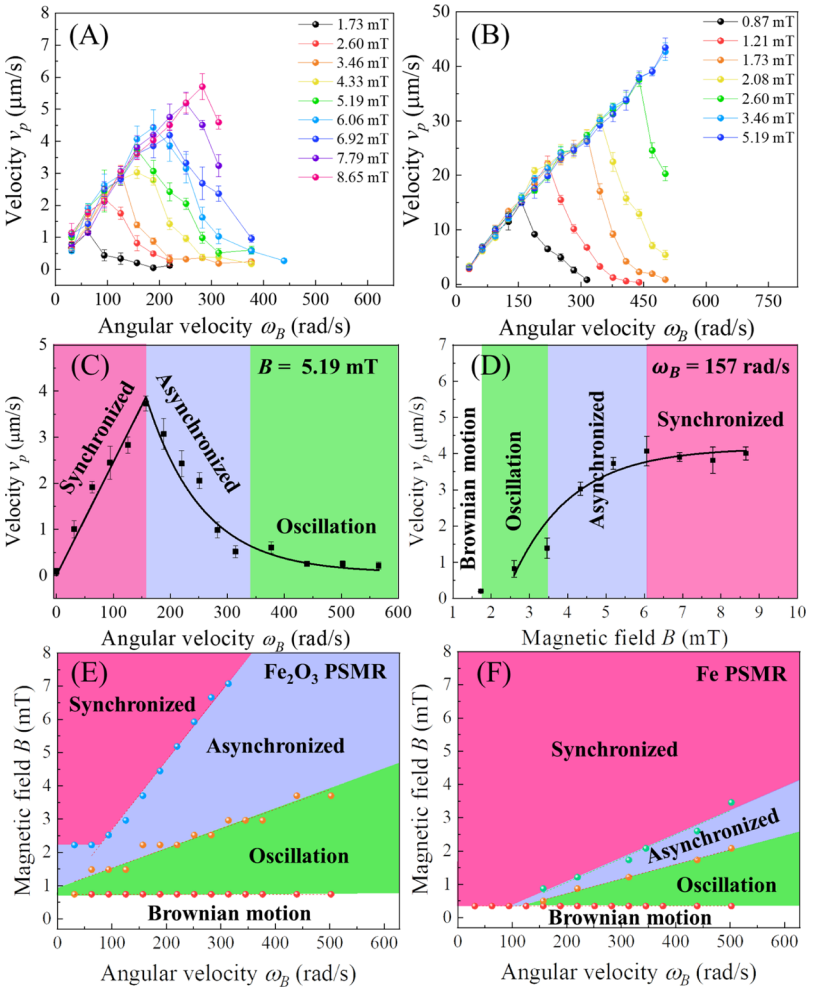

Figure 4. Plots of translational speed v_p vs ω_B for different magnetic fields B for (A) Fe_2O_3 PSMRs and (B) Fe PSMRs. The black dashed lines are a guide-of-eye, representing a linear relationship. The four motion zones based on (C) v_p–ω_B relationship for a fixed B, and (D) v_p–B relationship for a fixed ω_B. The data presented in (C,D) are for a Fe_2O_3 PSMR. The phase diagram of the motion behavior for (E) Fe_2O_3 PSMR and (F) Fe PSMR.

https://dx.doi.org/10.1021/acs.langmuir.0c02132
Langmuir 2020, 36, 11125−11137

shape and motion direction of the PSMR. In addition, the resistant matrix M_h has to be symmetric according to the reciprocal theorem of Stokes flow, that is, $c = b^{-1}$.[43] Table S1 summarizes the expression for the diagonal components of the resistant matrix component of a slender rod with different translational and rotational motion configurations in a bulk liquid,[42,44,45] while c and b can be calculated numerically based on an integration suggested by ref 46. The wall effect on these matrix components can only be estimated numerically.[43] The resistance matrix components for PSMR are even more complicated and cannot be expressed analytically. As a reasonable approximation, later we will use the expressions in Table S1 to estimate the hydrodynamic drag force and torque. Based on eqs 1−4, one can obtain the following equation

$$\omega_p = \dot{\beta} = M_s B \sin \omega_B t \sin \beta / D \tag{5}$$

where $D = d + br + \xi cr + \xi a r^2$. The general solution for eq 5 is determined by a critical angular speed ω_c[47,48]

$$\omega_c = \frac{M_s B}{D} \tag{6}$$

For $\omega_B < \omega_c$, the rotation of the PSMR can be synchronized with the frequency of the applied magnetic field, that is, $\omega_p = \omega_B$. When $\omega_B > \omega_c$, the rotation of the PSMR becomes asynchronous to the applied magnetic field because of the drastic increase of the liquid-induced viscous torque, and $\omega_p = \dot{\beta} = \omega_B - \sqrt{{\omega_B}^2 - {\omega_c}^2}$. According to eq 3, because $v_p \propto \omega_p$, the following is expected

$$v_p = \begin{cases} \xi r \omega_B, & \omega_B < \omega_c \\ \xi r(\omega_B - \sqrt{{\omega_B}^2 - {\omega_c}^2}), & \omega_B > \omega_c \end{cases} \tag{7}$$

Therefore, v_p is a function of both ω_B and B. Figure 4A,B shows the experimental data for the translational speed v_p versus ω under different B for the Fe_2O_3 PSMR and the Fe PSMR. Regardless of the PSMR motion configuration, the overall motion behaviors of the Fe_2O_3 PSMR and the Fe PSMR as a function of B and ω_B are similar. Similar relationships have been reported in the literature.[1,21,48] At a fixed B (Figure 4C), the v_p−ω_B relationship follows the following general trend: when ω_B is very small, the PSMR can hardly move and its motion is dominated by Brownian motion; when ω_B is sufficient but still small, the PSMR starts to rotate along with the provided ω_B, and directional translation motion of the PSMR is observed. In this case, the translational speed v_p is proportional to ω_B, and we call this synchronized motion; then, v_p reaches a maximum v_{max} at a certain ω_B value, $\omega_B = \omega_c$. When ω_B increases further, although the PSMR still moves translationally, other mixed motion modes are observed (see the Supporting Information Movie M4). For example, for the rolling of the Fe_2O_3 PSMR, tumbling in different orientations were observed. The randomly appearance of different motion modes effectively reduces v_p, that is, v_p decreases monotonically with ω_B. In this case, the rotation of the PSMR is not synchronized with ω_B, as shown in eq 7. After ω_B exceeds another threshold value, the PSMR only oscillates almost at the same location (see the Supporting Information Movie M5), and v_p diminishes (Figure 4C). Similarly, if ω_B is fixed and when the v_p−B relationship is investigated, the four zones are observed: Brownian, synchronized, asynchronized, and oscillation zones. As shown in Figure 4D, when B is very small, only Brownian motion can be observed; with the increase of B, the PSMR first starts to oscillate, then moves asynchronized with the external field, and finally the motion is synchronized at a sufficiently large B. Although these general trends are all very similar for both Fe_2O_3 PSMR and Fe PSMR, the values of v_p, ω_c, and the changing rate are very different. For example, under the same magnetic field, the v_{max} and ω_c for the Fe_2O_3 PSMR and Fe PSMR are significantly different. For instance, when B = 1.73 mT, $v_{max}^{Fe_2O_3}$ is smaller than 2 μm/s, while the value of v_{max}^{Fe} can go up to 25 μm/s. In addition, $\omega_c^{Fe_2O_3} = 62.8$ rad/s, which is significantly smaller than $\omega_c^{Fe} = 314$ rad/s, that is, the Fe PSMR not only has higher v_p values under the same B and ω_B conditions, but also has a larger linear v_p−ω_B tunability. Based on the above discussion and data obtained from Figure 4A,B, phase diagrams of the motion behavior of the PSMRs can be obtained. Figure 4E,F shows the corresponding phase diagram. Compared to the Fe_2O_3 PSMRs, the synchronized zone (pink area, $0 < B \leq 8$ mT and $0 < \omega_B \leq 625$ rad/s) dominates the phase diagram of the Fe PSMRs, and the other three zones are significantly smaller. This indicates that the Fe PSMRs can easily achieve synchronized motion at low magnetic field and high frequency, that is, the tumbling motion has a large flexibility to achieve synchronized motion. Thus, they require smaller magnetic field, can easily reach a higher speed at a larger frequency, and are ideal to use for controlled micro-/nanomotor applications.

Based on eq 7, one can extract the slipping coefficient for Fe_2O_3 PSMRs and Fe PSMRs. Both panels A and B of Figure 4 show that when $\omega_B < \omega_c$, the linear v_p−ω_B relationships for different B are almost overlapped with each other. An average slope can be extracted from each plot, and we obtained that $k^{Fe_2O_3} = \xi^{Fe_2O_3} r^{Fe_2O_3} = 0.022 \pm 0.002$ μm/rad and $k^{Fe} = \xi^{Fe} r^{Fe} = 0.093 \pm 0.002$ μm/rad. Also, note that $r^{Fe_2O_3} = d_1/2$ and $r^{Fe} = l/2$, we obtained that $\xi^{Fe_2O_3} = 0.0249 \pm 0.0008$ and $\xi^{Fe} = 0.051 \pm 0.002$, that is, $\xi^{Fe} \approx 2\xi^{Fe_2O_3}$. According to eqs 1 & 4, $F_f = av_p + b\omega_p$, and it is reasonable to assume that $av_p > b\omega_p$, so that $F_f \sim av_p$. According to Table S1, $a^{Fe_2O_3} = a_\perp = \frac{4\pi\eta l}{\ln(2\gamma) + 0.5} = 2.22 \times 10^{-8}$ N m^{-1} s, while $a^{Fe} = \frac{a_\perp + a_\parallel}{2} = \frac{\pi\eta l'}{\ln(2\gamma) - 0.5} + \frac{2\pi\eta l'}{\ln(2\gamma) + 0.5} = 2.33 \times 10^{-8}$ N m^{-1} s (see Section S7 in the Supporting Information), that is, $a^{Fe_2O_3} \approx a^{Fe}$. Note that $k^{Fe} \approx 4k^{Fe_2O_3}$ implies that under the same B and ω_B, the tumbling motion can induce a four times larger friction than that of the rolling motion, thus achieving a four times faster speed.

The parameter D can be estimated by investigating how ω_c changes with B (eq 6, here we assume that M_s is a constant, i.e., the FSMR was not magnetized or demagnetized during the experiments). Figure S7 shows the plots of the ω_c−B relationships for both the Fe_2O_3 PSMRs and the Fe PSMRs extracted from Figure 4A,B. A linear fit can extract the slopes $\frac{M_s^{Fe_2O_3}}{D^{Fe_2O_3}} = 32.5 \pm 0.6$ rad/mT·s and $M_s^{Fe}/D^{Fe} = 174 \pm 4$ rad/mT·s. Therefore, we obtain $D^{Fe_2O_3} = 1.6 \times 10^{-19}$ N·m·s and $D^{Fe} = 8.56 \times 10^{-18}$ N·m·s experimentally. If both the Fe_2O_3 PSMR and the Fe PSMR are rotating in a bulk liquid, the D in eq 6 will be replaced by $d^{Fe_2O_3} = d_\perp = \frac{\pi\eta l^3\left(1 + \frac{0.677}{\gamma} - \frac{0.183}{\gamma^2}\right)}{0.96\,\gamma^2} = 4.11 \times 10^{-20}$ N·m·s, and $d^{Fe} = d_\parallel = \frac{\pi\eta l'^3}{3\left(\ln\gamma - 0.662 + \frac{0.917}{\gamma} - \frac{0.05}{\gamma^2}\right)} = 8.72 \times 10^{-20}$ N·m·s. Clearly the experimentally obtained $D^{Fe_2O_3}$ is one

https://dx.doi.org/10.1021/acs.langmuir.0c02132
Langmuir 2020, 36, 11125−11137

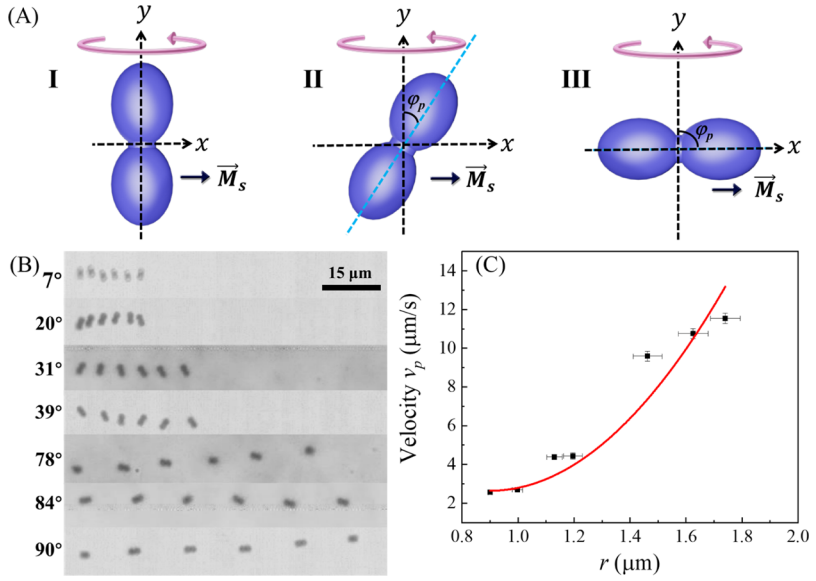

Figure 5. (A) Cartoons for synchronized motion of PSMRs with different magnetic moment orientations. (B) Time-lapse movie images of PSMRs with different φ_p within 6 s under a nuAMF of B = 3.46 mT and f_B = 15 Hz (ω_B = 94.2 rad/s). (C) Plot of v_p of PSMRs with different φ_p vs r. The red curve is the fitting result.

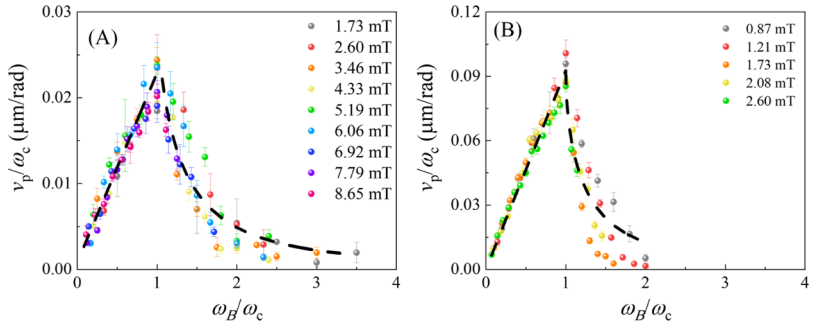

Figure 6. Rescaled plots of v_p/ω_c vs ω_B/ω_c for (A) Fe_2O_3 PSMRs and (B) Fe PSMRs. Black dash lines are the fittings based on eq 7.

order of magnitude larger than $d^{Fe_2O_3}$, while D^{Fe} is two orders of magnitude larger than d^{Fe}. This means that other factors significantly alter the hydrodynamic torque, in particular, the wall effect and the friction-induced torque.

The above results show that when the magnetic moment orientation φ_M takes two extreme cases, that is, perpendicular (φ_M = 90°) or parallel (φ_M = 0°) to the long axis of the PSMR, two significant motion behaviors (rolling and tumbling) are observed. A natural question is: if the φ_M changes continuously from 90 to 0°, how would the motion behavior change? Here, one needs to find a way to continuously tune the orientation of M_s while keeping the size and the shape of PSMR. Fortunately, during the PSMR preparation, we found that the reduction time could be used to tune the φ_M, especially when the reduction time was 2 h, there was a broad distribution of φ_M, see Figure S10B. Based on the XRD result shown in Figure S11, the sample was a mixture of Fe_3O_4 and Fe. Therefore, we could selectively pick up PSMRs with different φ_M during the motion experiment. The motion movies of the PSMRs were taken first by applying a DC magnetic field so that the φ_M of each individual PSMR could be determined and then by switching to a nuAMF. Note that we do not know the actual magnitude of M_s for each PSMR. The Supporting Information Movie M8 shows the motions of 7 PSMRs with φ_p = 7, 20, 31, 39, 78, 84, and 90°, respectively, under B = 3.46 mT and f_B = 15 Hz for the same period of time t = 6 s, and the time-elapse movie frames in every second are shown in Figure 5B. The φ_p–φ_M relationship is plotted and shown in Figure S12, and two conclusions can be reached: first, the slope is 1.16 ± 0.02, very close to 1, so the precession angle φ_p increases linearly with φ_M. Second, there is a non-zero intercept, that is, when φ_M = 0°, φ_p = 7°. This small φ_p indicates that even at φ_M = 0°, the motion is ill slightly precession. In addition, from Figure 5, two general features can be seen: first, the PSMRs with 0 < φ_p < 90° all undergo precession motions; and second the larger the φ_p, the larger the translational distance the PSMRs move, that is, the v_p increases monotonically with φ_p. According to eq 3, v_p is proportional to the precession radius r of the PSMRs. Both v_p and r can be extracted directly from the Supporting Information Movie M8, and Figure 5C shows the plots of the v_p versus r. Although a linear fitting could result in a good data match, it gives a negative intercept (−7 ± 1 μm/s) at r = 0 μm, which is not physically feasible. As discussed previously, $\xi^{Fe} \approx 2\xi^{Fe_2O_3}$, that is, the slipping coefficient is also a function of the orientation of M_s or r. This is because the hydrodynamics of PSMRs with a different precession angle is different, that is, the local flow-induced pressure of PSMRs with a different precession angle is different, which is a function of r. This indicates that the interaction between the PSMRs and the substrate is different, and infers that the slipping coefficient ξ is

https://dx.doi.org/10.1021/acs.langmuir.0c02132
Langmuir 2020, 36, 11125−11137

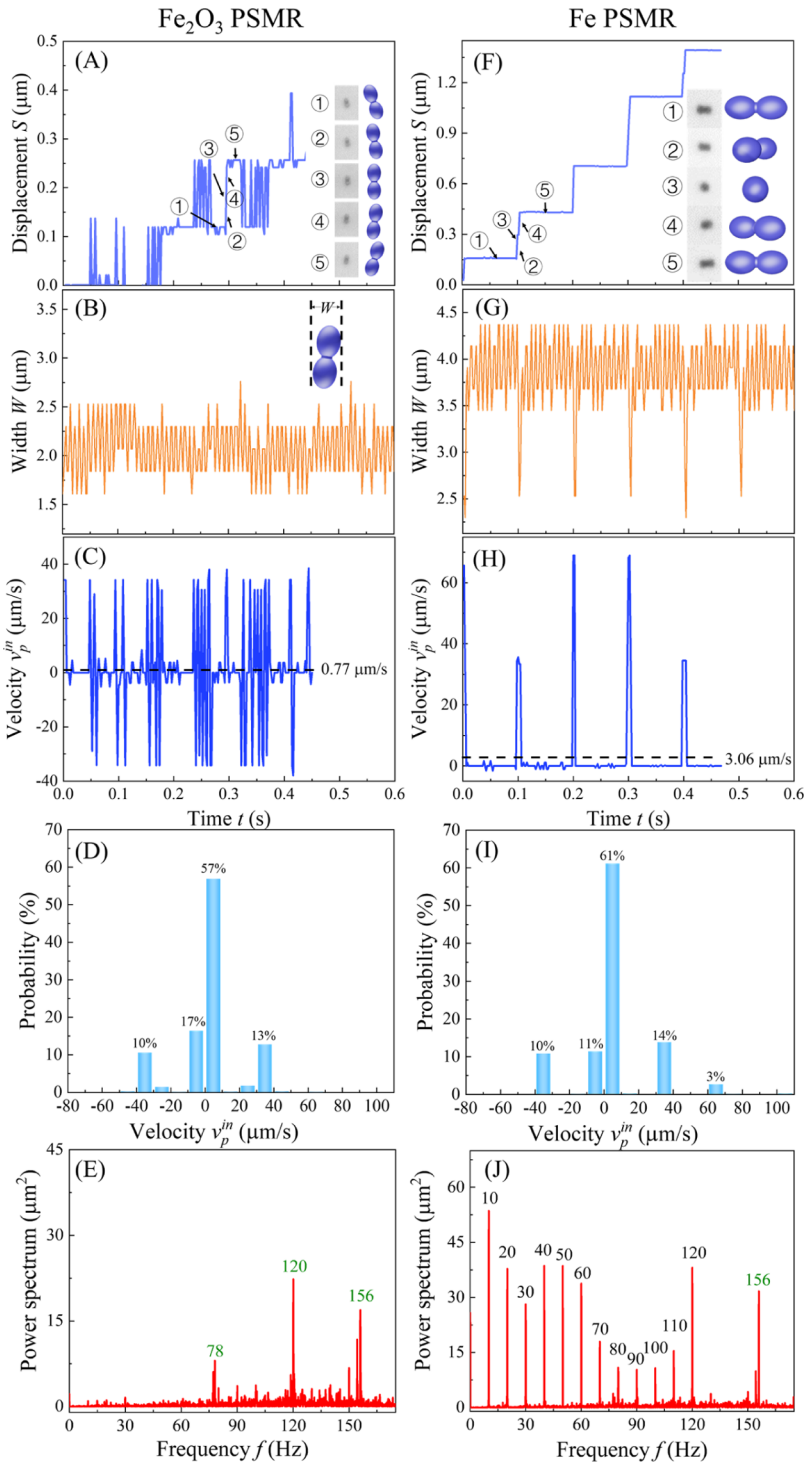

Figure 7. Detailed motion analysis of the PSMRs under a nuAMF of B = 3.46 mT and f_B = 5 Hz (ω_B = 31.4 rad/s) recorded at 500 fps. For a Fe_2O_3 PSMR: (A–C) plot the displacement S, projected width W, and velocity v_p vs time t; (D) instant velocity v_p^{in} distribution; and (E) power spectrum of v_p^{in}. For a Fe PSMR, (F) S vs t, (G) W vs t, (H) v_p vs t, (I) v_p^{in} distribution, and (J) power spectrum of v_p^{in}.

not a constant. We use the following quadratic function to the v_p–r relationship, $v_p = \varepsilon(r - r_0)^2 + v_0$, where $r_0 = r(\varphi_p = 0°)$ and $v_0 = v(\varphi_p = 0°)$. The best fitting gives $\varepsilon = 15 \pm 2\ \mu m^{-1}\cdot s^{-1}$, $r_0 = 0.9\ \mu m$, and $v_0 = 2.6 \pm 0.2\ \mu m/s$, which better describes the fact that the rolling motion gives the minimum velocity v_0.

Scaling Behavior of Magnetic MSWs. In most micro-/nanomotor works, the moving performances are characterized by the speed to body length ratio, v_p/l.[33] For example, the highest v_p/l reported so far in the literature is ~260,000 body-length/s of optically propelled ballistic plasmonic Au nanoparticle swimmers with an unprecedented velocity of ~336,000 μm/s.[49] However, for magnetic micro-/nanomotors, its v_p not only depends on the driving field B, but also the driving frequency f_B. Thus, in order to establish a parameter that can uniquely describe the motion performance of the magnetic motors, one needs to normalize the motion behavior out of these two external factors. As shown in Figure 4A,B, the behavior of v_p–ω_B is determined by ω_c, while ω_c is

https://dx.doi.org/10.1021/acs.langmuir.0c02132
Langmuir 2020, 36, 11125–11137

proportional to B, thus it is reasonable to rescale Figure 4A,B by plotting v_p/ω_c versus ω_B/ω_c (where $\omega_c = \omega_c^{Fe_2O_3}$ for the Fe_2O_3 PSMR and $\omega_c = \omega_c^{Fe}$ for the Fe PSMR). Figure 6A,B shows the corresponding rescaled plots. After scaling, all of the $v_p/\omega_c - \omega_B/\omega_c$ curves are collapsed together. The dashed lines and curves are fits according to eq 7. Clearly, the general scaled $v_p/\omega_c - \omega_B/\omega_c$ relationship for a rotating magnetic motor is very similar, regardless of the magnetic moment orientation. Such a scaling relationship should also be observed for the data reported in the literature.[1,21,48] Therefore, based on the speed to body length ratio that is generally used to characterize micro-/nanomotors and the two external factors B and f_B unique to magnetic motors (similar for external electric field driven motors, etc.), we can define a new quality parameter q_m

$$q_m = \frac{v_p}{lB\omega_B} = \frac{\xi r \omega_p}{lB\omega_B} \tag{8}$$

that can be used unbiasedly to quantify the translational motion of a magnetic micro-/nanomotor, where l can be interpreted as the largest length scale of the particle. Based on Figure 4 and eq 7, for the same particle, the synchronized motion ($\omega_B < \omega_c$ and $\omega_p = \omega_B$) gives a higher q_m

$$q_m = \frac{r}{l}\frac{\xi}{B} \tag{9}$$

In addition, because $2r \leq l$, given the same ξ and B, the tumbling motion, that is, $2r = l$, always gives the best translational performance. Table S2 summarizes some typical q_m of magnetic motors extracted from the literature and our current work. The tumbling motion observed for our magnetized Fe PSMRs gives the maximum q_m (= 25.48 T^{-1}), while the rolling motion of the magnetized Fe_2O_3 PSMRs has a q_m (= 2.39 T^{-1}), which is one order of magnitude smaller. In the literature, most motions of magnetically propelled micro-/nanomotors have $q_m < 10$, only the motions of micromagnetic helical motors fabricated by three-dimensional direct laser writing[50] and Janus micro-dimer swimmers[28] can achieve a relative high q_m value, 13.65 and 13.24 T^{-1}, respectively. Thus, it is still very challenging to design magnetic micro-/nanomotors with a high q_m value.

Nature of the Discretized Motions of MSWs. So far, in the literature, the motion behaviors of almost all MSWs (similar to those listed in Table S2) were interpreted by continuum hydrodynamics at low Reynolds number. However, if one takes the tumbling motion of a Fe PSMR as an example and considers the free body diagram in Figure 3B carefully, one would notice that at different phases of the rotatory motion of the PSMR, the interaction between the PSMR and the substrate is different: when one end of the PSMR is pointing downward to the substrate surface, the gap between the PSMR and the substrate is minimum, and one expects a strong PSMR−wall interaction; but, when the PSMR is lying horizontal above the substrate, the gap between the PSMR and the substrate is maximum, and the PSMR−wall interaction is minimum. In fact, in our previous publication,[27] the numerical simulation showed that the translational displacement of a tumbling magnetic spheroid under a nuAMF is stepwise: at the time when the OMF changes its direction, the long axis of the PSMR is aligned with the magnetic field and the magnetic torque is close to zero while the magnetophoretic force difference at the two ends is maximized, which starts to rotate the PSMR clockwise. Once the PSMR deviates from the horizontal direction, a nonzero magnetic torque appears to further rotate the PSMR clockwise. During the rotation, the hydrodynamic interaction between the PSMR and the substrate generates the friction force f to move the PSMR translationally. Such a rotation only happens in a short period of time. After realigning the PSMR with the magnetic field (half revolution), the PSMR would stay aligned without rotation or translation, until a later time when the magnetic field changed its direction again. According to the numerical simulation, this rotation and translation happens at $0.15T$ and $0.65T$.[27] Because there were two instances when the magnetic field would change direction in one magnetic field oscillation period, consequently, the PSMR would perform two half-revolution rotations and move stepwise twice within one oscillation period. Thus, both the rotation of the PSMR and the translational velocity are discretized (see Figures 10 and 11 in ref 27). If the PSMR is rotated at a frequency f_p, the nonzero v_p occurs at a frequency of $2f_p$. In order to see whether the motion of a tumbling PSMR processes above-mentioned features, we have reinvestigated the motion behaviors of both Fe_2O_3 PSMRs and Fe PSMRs under a nuAMF of B = 3.46 mT and f_B = 5 Hz but the CCD recoding speed was set at 500 fps, that is, 100 times f_B (see the Supporting Information Movie M9). Figure 7 shows the detailed motion analysis for these two kinds of particles. For a Fe_2O_3 PSMR, although the overall envelop displacement curve looks similar to a staircase function, there are many displacement fluctuations (Figure 7A). The apparent width W of the PSMR (Figure 7B) also fluctuates fairly randomly between 1.5 to 2.5 μm, which is consistent with the d_1 (= 1.7 μm) value of the Fe_2O_3 PSMR and is an indication of a rolling-like motion. The instantaneous velocity $v_p^{in}-t$ plot (Figure 7C) shows a randomly fluctuated v_p^{in} distribution between 35 and −35 μm/s. Figure 7D shows the plots of the corresponding probability distribution of v_p^{in}. Evidently, most v_p^{in} are distributed at 0 and ±35 μm/s. This discretized velocity is the result of the digital nature of the CCD camera because it only has an image resolution of one pixel for determining the displacement. Figure 7D shows that about 74% probability of v_p^{in} is distributed around 0 μm/s; 10% of v_p^{in} is centered around −35 μm/s; and 13% of v_p^{in} is distributed around 35 μm/s. The slightly higher probability at 35 μm/s gives an overall average velocity as 0.77 μm/s, which is consistent with the value (~0.7 μm/s) shown in Figure 4A. Figure 7E shows the power spectrum of $v_p^{in}(t)$, which gives the frequency characteristics of the motion. Three sharp distinguished peaks at f = 78, 120, and 156 Hz are observed, which are not intrinsic to our experiment. Rather, they are due to the line frequency (120 Hz) and unknown sources (78 and 156 Hz). They are presented in almost all our spectra when the CCD frame rate is large enough. The Fe PSMR shows a completely different behavior. A staircase-like displacement curve is observed as shown in Figure 7F: from one step to the nearest neighbor step, the displacement increment is 0.31 ± 0.04 μm. Also, the corresponding movie snapshots and cartoons of the Fe PSMR configuration are shown as an insert in Figure 7F and are indicated by the corresponding time spots on the displacement curve. The displacement increment occurs between configurations ② and ④, when the PSMR states to rotate, which was predicted exactly by ref 27. The $W-t$ plots in Figure 7G indicate that at most times, the W is about 3.5−4.5 μm, which is consistent with the length l (= 3.48 μm) of the Fe PSMR. This implies that at most times, the PSMR neither rotates nor moves translationally. However, at the time when

https://dx.doi.org/10.1021/acs.langmuir.0c02132
Langmuir 2020, 36, 11125−11137

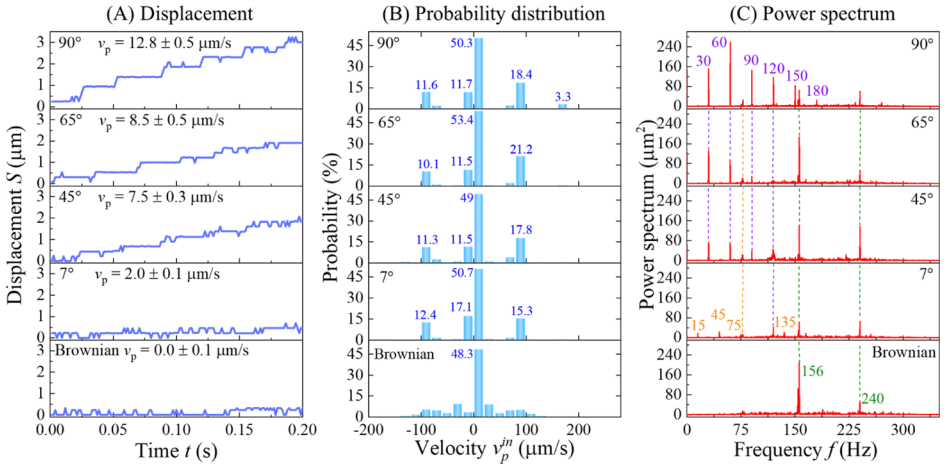

Figure 8. Detailed motion analysis of the PSMRs with φ_p = 7, 45, 65, and 90° under a nuAMF of B = 3.46 mT and f_B = 15 Hz recorded at 750 fps. The corresponding plots for Brownian motion are added for reference: (A) displacement S vs time t, (B) probability distribution of v_p^{in}, and (C) power spectrum of $v_p^{in}(t)$.

the PSMR moves translationally up a step, W reduces significantly to ~2.5 μm, that is, the d_1 value of the PSMR indicates an instantaneous rotation occurring. Higher speed movie analysis (taken at 5000 fps, see Section S9 of the Supporting Information) shows that the time duration for this rotation is about 0.01 s, compared to the period T = 0.2 s. The v_p^{in}–t plot as shown in Figure 7H is a comb function, with a discretized nonzero v_p^{in} appearing in every half period. The corresponding v_p^{in} distribution is shown in Figure 7I. Still around 72% of v_p^{in} is distributed around 0 μm/s, 10% at −35 μm/s, 14% at 35 μm/s, and 3% at 115 μm/s. There is a significant higher probability of positive velocity distribution at 35 and 65 μm/s, respectively, which results in an average velocity of 3.06 μm/s (the corresponding value in Figure 4B is ~3 μm/s). In addition, Figure 7J shows a comb-like power spectrum of $v_p^{in}(t)$ with evenly spaced sharp spectral peaks starting at a fundamental frequency f_0 = 10 Hz. Other sharp peaks are located at higher order harmonics of f_0. Note that the rotation frequency of the Fe PSMR is f_B = 5 Hz, that is, f_0 = $2f_B$, which was predicted exactly by our previous publication,[27] and that the nature of the discretized tumbling motion of the Fe PSMR is independent of the CCD frame rate (see Section S10 of the Supporting Information).

The above observations reveal the following characteristics of a MSW: (1) in about 70% of the time, the v_p of the PSMR is zero, that is, there is no translational driving force; thus, during that period of time, the PSMR performs neither translational motion nor rotary motion; (2) a translational motion occurs simultaneously only when the PSMR rotates. During the rotation, the pressure difference between the two sides of the end of the PSMR produces an instantaneous driven force, that is, a friction force. This friction force and corresponding toque would be the cause to move the particle forward,[27] and such an interaction only happens in a very short time period; (3) the tumbling motion is more regular or predictable than the rolling motion. Therefore, eqs 1 & 2 shall be changed to discretized formats. For example, for the tumbling motion of the Fe PSMR, they become

$$\begin{cases} F_f - F_h = 0 \\ -\tau_M + \tau_h + rF_f = 0 \end{cases}, \quad \frac{n}{2}T + 0.15T - \frac{\delta}{2} < t < \frac{n}{2}T + 0.15T + \frac{\delta}{2}, \quad n = 0, 1, 2, \ldots \tag{10}$$

where δ is the instantaneous rotation time duration, and $T = 2\pi/\omega_p$ is the period of rotation. According to our previous simulation, for the synchronized motion, let us assume that $F_h = Av_p^{in} = A\xi r\omega_p^{in}$ and $\tau_h = D\omega_p^{in}$, where A and D are the instantaneous hydrodynamic drag and torque coefficient, respectively, and v_p^{in} and ω_p^{in} are the instantaneous translational velocity and angular frequency, respectively, when the end of the Fe PSMR is pointing to the substrate. Thus, during $\frac{n}{2}T + 0.15T - \frac{\delta}{2} < t < \frac{n}{2}T + 0.15T + \frac{\delta}{2}$, the ω_p^{in} can be solved as

$$\omega_p^{in} = \frac{2M_sB\sin(0.3\pi)}{\pi(D + \xi Ar^2)} \tag{11}$$

the v_p^{in} can be expressed as

$$v_p^{in} = \frac{2M_sB\xi r\sin(0.3\pi)}{\pi(D + \xi Ar^2)} \tag{12}$$

and the average velocity v_p is

$$v_p = \frac{\delta}{T}\frac{4M_sB\xi r\sin(0.3\pi)}{\pi(D + \xi Ar^2)} = \frac{\delta\omega_p}{\pi^2}\frac{2\sin(0.3\pi)M_sB\xi r}{(D + \xi Ar^2)} \tag{13}$$

Equation 13 gives the PSMR velocity we measured in previous sections (or those reported in the literature), and it reveals a complicated relationship among the geometry and magnetic property of the particle, the hydrodynamic interactions, and the applied magnetic field. First, the average v_p is proportional to both M_s and B as well as the average particle rotation frequency ω_p. The geometric parameters of the particle and the hydrodynamic interaction are expressed inseparably in the expression, $\frac{\xi r}{D + \xi Ar^2}$. Here, the parameters ξ, A, and D are not only determined by the hydrodynamics due to the shape of the particle, but also the particle to substrate

https://dx.doi.org/10.1021/acs.langmuir.0c02132
Langmuir 2020, 36, 11125−11137

distance. The parameter δ is the time duration when the particle and the substrate have a strong interaction. Thus, the quality factor for a PSMR can be expressed as

$$q_m = \frac{\delta}{\pi^2}\frac{2\sin(0.3\pi)M_s\xi r}{(D+\xi Ar^2)l} \quad (14)$$

which shows that q_m is determined by the shape of the PSMR and the hydrodynamics near a wall as well as the magnetic property of the MSW. In order to achieve a high q_m, one should satisfy the following: (1) the motion mode should be tumbling motion, that is, $r = l/2$. (2) The magnetic moment of the PSMR M_s should have a large value, that is, to fabricate a PSMR with a material that has high M_r. One should notice that for the motions of PSMRs shown in Figures 2 and 4, the PSMRs were magnetized under a 1.5 T magnetic field, which means the corresponding M_s value was maximized. For the nonmagnetized Fe_2O_3 and Fe PSMRs, as discussed in Section S11 of the Supporting Information, under the same nuAMF condition, their v_p are significantly smaller than those shown in Figure 4. In fact, the q_m for the nonmagnetized Fe_2O_3 and Fe PSMRs are 0.89 and 11.53 T^{-1}, respectively, which are significantly smaller than the values of the magnetized PSMRs. (3) The MSW−substrate interaction time δ should be high. This can be achieved by introducing roughness or a rachet surface on the substrate,[21] or by changing the shape of the MSW by introducing multiple branches. (4) The hydrodynamic interaction near a wall, $\frac{\xi}{D+\xi Ar^2}$, should be increased. This is rather complicated because one not only needs to consider the shape of the MSW, but also instantaneous hydrodynamics near a wall.

Another important question regarding the discretized motion behavior is: How does the discretized motion depend on φ_M? Figure 8 shows some representative motion characterizations, the $S-t$ curve, the probability distribution of v_p^{in}, and the power spectrum of $v_p^{in}(t)$ of PSMRs with φ_p = 7, 45, 65, and 90°, respectively, under a nuAMF of B = 3.46 mT and f_B = 15 Hz recorded at 750 fps. The Brownian motion behavior captured under the same condition is also presented as a reference. The $S-t$ curves shown in Figure 8A clearly indicate that as φ_p increases, the shape of the $S-t$ curves looks more and more similar to a staircase function, especially for $\varphi_p \geq$ 65°. The slope of the $S-t$ curve increases monotonically with φ_w, which is consistent with the result shown in Figure 5C. The v_p^{in} probability distribution shown in Figure 8B indicates some very interesting trends: (1) regardless of φ_p, most of the v_p^{in} are distributed at 0, ±90 μm/s; the Brownian motion has a rather symmetric distribution with the highest probability (= 48.3%) at v_p^{in} = 0 μm/s; (2) the probability of v_p^{in} at 0 μm/s is about the same between 60 and 68%, which is consistent with the results from Figure 7, that is, in about 60%−68% time, the PSMRs perform neither translational motion nor rotary motion; (3) the probability difference of v_p^{in} = 90 μm/s and v_p^{in} = −90 μm/s increases monotonically, from 2.9% at φ_p = 7°, to 6.5% at φ_p = 45°, and to 11.1% at φ_p = 65°. At φ_p = 90°, this difference is only 7.8%, but there is an extra 3.3% probability occurring at v_p^{in} = 170 μm/s, which is equivalent to 6.6% difference. This makes the probability difference total to 14.4%. Clearly, with the increase of φ_p, the v_p^{in} distribution is more biased toward positive v_p^{in}. The quality of the staircase motion can be characterized by the power spectrum of $v_p^{in}(t)$ as shown in Figure 8C. The power spectrum of Brownian motion indicates two characteristic peaks at f = 156 and 240 Hz. These peaks are present in all of the spectra. For φ_p = 7°, one can see small, sharp discretized peaks at f = 15, 45, 75, and 135 Hz, that is, $f_0 = f_B$ = 15 Hz, which is not a characteristic of the discretized motion reported in ref 27. When φ_p increases to 45°, sharp peaks occur at f = 30, 60, and 90 Hz, that is, f_0 = 30 Hz or $f_0 = 2f_B$. This shows that the discretized features start to appear, but only the second and third harmonics can be observed. Similar spectral features are observed for φ_p = 65°, the only difference is that the peak intensities at f_0 and the two harmonics increases. However, for φ_p = 90°, more harmonic peaks at f = 120, 150, and 180 Hz are observed. Clearly, the PSMR at φ_p = 90° has the highest quality of discretized motion. This conclusion can be further drawn from the plot of the power at f_0 = 30 Hz versus φ_p, as shown in Figure 9. It

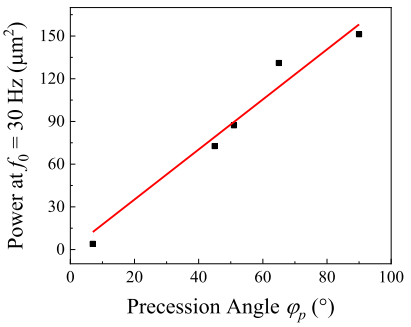

Figure 9. Plot of the power at f_0 = 30 Hz of $v_p^{in}(t)$ vs precession angle φ_p. The red line is a linear fitting.

exhibits a linear relationship, demonstrating that for φ_p = 90°, one obtains the best double frequency motion. The above results clearly demonstrate that the precession motion should also exhibit the discretized motion feature when φ_p is large enough. However, when φ_p is close to 0°, at any location of the PSMR, the distance variation between the PSMR and the substrate is very small. Thus, the PSMR will feel a small constant and continuum driving force induced by the rotation, so no discretized motion features can be observed. Clearly the discretized motion of PSMRs only depends on the motion configuration of the PSMR: the rolling motion does not induce an obvious discretized motion while the precession motion or the tumbling motion exhibits the discretized motion. In addition, the motion configurations depend on the direction of the magnetic moments of the PSMRs. According to the phase diagram shown in Figure 4F, for the Fe PSMRs and in the synchronized motion region, regardless of the magnetic field magnitude and the applied frequency, the Fe PSMRs perform tumbling motion and their motion is discretized.

CONCLUSIONS

In summary, we have shown that the orientation of the magnetic moment of a magnetic micro-/nanomotor has a significant influence on the motion mode under a nuAMF. By changing the reduction condition, we fabricated PSMRs with different M_s orientations. When gradually changing φ_M from 90° (perpendicular to the long axis of the PSMR) to 0°, the motion of the PSMR evolves from rolling to precession, then to tumbling. Systematic investigations on the dependence of the translational velocity v_p on the magnitude of the applied magnetic field B and oscillation frequency ω_B show that the overall motion of the PSMRs can be divided into four different zones: Brownian motion zone, synchronized zone, asynchron-

https://dx.doi.org/10.1021/acs.langmuir.0c02132
Langmuir 2020, 36, 11125−11137

ized zone, and oscillation zone. Under the synchronized motion condition and with the same external field, the translational motion velocity increases monotonically with φ_P. Regardless of the φ_P, the synchronized zone is favored for real applications, and the size of this zone depends on the orientation of M_s. The tumbling motion of Fe PSMRs has a much larger synchronized zone than that of the Fe_2O_3 PSMRs. The $\nu_p-\omega_B$ relationship can be rescaled by a critical angular frequency ω_c, which is determined by M_s, B, and a hydrodynamic term D. This indicates that there should be an intrinsic quality factor q_m to characterize the translational motion of MSWs. We have compared the quality factors of our current work with those reported in the literature and found that q_m ranged from 0.73 to 13.65 T^{-1}. The Fe PSMR in the current work gave the highest q_m (= 25.48 T^{-1}). In addition, high speed movies revealed that both the tumbling and precession motions of the PSMRs processed a discretized nature and their displacement versus time curve followed a staircase function while their instantaneous velocity versus time curve is a comb function with a frequency doubling the rotation frequency of the MSW. The strong hydrodynamic wall effect during the instantaneous rotation of the PSMR would impose a driving force to move the particle translationally. By analyzing this discretized motion, an analytic expression for q_m is obtained and is found to be determined by the shape of the MSW, the hydrodynamics near a wall, and the magnetic property of the MSW. By analyzing factors influencing q_m and based on the experimental observations, we discovered that the tumbling motion of the PSMRs can give the best discretized motion, and therefore, the best q_m. Suggestions on motor design or substrate surface design were given based on the expression for q_m. This work can help researchers to better understand the motion of MSWs and gain insight into designing better micro-/nanomotors for different applications.

■ ASSOCIATED CONTENT

Supporting Information

The Supporting Information is available free of charge at https://pubs.acs.org/doi/10.1021/acs.langmuir.0c02132.

Motion configurations of magnetic rod particles; magnetic and motion observation setup; volume calculation of PSMRs; estimated volume change due to the change from a Fe_2O_3 PSMR to a Fe PSMR; precession of the long axis of the Fe_2O_3 PSMRs during rolling motion; slipping coefficient; calculation of the a^{Fe} component in "resistance matrix"; characterization of 2 h annealed PSMRs; high speed movie analysis; motion recordings with different CCD frame rates; plots of ν_p versus ω_B for nonmagnetized Fe_2O_3 and Fe PSMRs; expressions for the resistant matrix components; and summary of q_m (PDF)

Synchronized motion of a Fe_2O_3 PSMR (AVI)

Synchronized motion of a Fe PSMR (AVI)

Asynchronized motion of a Fe_2O_3 PSMR (AVI)

Oscillation of a Fe_2O_3 PSMR (AVI)

Asynchronized motion of a Fe PSMR (AVI)

Oscillation of a Fe PSMR (AVI)

Synchronized motion of PSMRs with different magnetic moment orientations (AVI)

Fast CCD movies of a Fe_2O_3 PSMR and a Fe PSMR (AVI)

■ AUTHOR INFORMATION

Corresponding Author

Yiping Zhao − *Department of Physics and Astronomy, The University of Georgia, Athens, Georgia 30602, United States;* orcid.org/0000-0002-3710-4159; Email: zhaoy@uga.edu

Author

Yanjun Yang − *School of Electrical and Computer Engineering, College of Engineering, The University of Georgia, Athens, Georgia 30602, United States;* orcid.org/0000-0002-1822-7364

Complete contact information is available at: https://pubs.acs.org/10.1021/acs.langmuir.0c02132

Notes

The authors declare no competing financial interest.

■ ACKNOWLEDGMENTS

This work is supported by the National Science Foundation under the contract no. ECCS-1808271. We would like to thank Yoong Sheng Phang for proofreading this manuscript.

■ ABBREVIATIONS

PSMRs, peanut-shaped magnetic microrods; nuAMF, nonuniform alternating magnetic field; MSW, magnetic surface walker; RMF, rotating magnetic field; OMF, oscillating magnetic field

■ REFERENCES

(1) Lin, Z.; Fan, X.; Sun, M.; Gao, C.; He, Q.; Xie, H. Magnetically Actuated Peanut Colloid Motors for Cell Manipulation and Patterning. *ACS Nano* **2018**, *12*, 2539−2545.

(2) Zhu, L.; Huang, W.; Yang, F.; Yin, L.; Liang, S.; Zhao, W.; Mao, L.; Yu, X.; Qiao, R.; Zhao, Y. Manipulation of Single Cells Using a Ferromagnetic Nanorod Cluster Actuated by Weak AC Magnetic Fields. *Adv. Biosyst.* **2019**, *3*, 1800246.

(3) Tang, J.; Yao, C.; Gu, Z.; Jung, S.; Luo, D.; Yang, D. Super-Soft and Super-Elastic DNA Robot with Magnetically Driven Navigational Locomotion for Cell Delivery in Confined Space. *Angew. Chem., Int. Ed.* **2020**, *59*, 2490−2495.

(4) Sun, M.; Fan, X.; Meng, X.; Song, J.; Chen, W.; Sun, L.; Xie, H. Magnetic Biohybrid Micromotors with High Maneuverability for Efficient Drug Loading and Targeted Drug Delivery. *Nanoscale* **2019**, *11*, 18382−18392.

(5) Qiu, F.; Fujita, S.; Mhanna, R.; Zhang, L.; Simona, B. R.; Nelson, B. J. Magnetic Helical Microswimmers Functionalized with Lipoplexes for Targeted Gene Delivery. *Adv. Funct. Mater.* **2015**, *25*, 1666−1671.

(6) Wang, X.; Hu, C.; Schurz, L.; De Marco, C.; Chen, X.; Pané, S.; Nelson, B. J. Surface-Chemistry-Mediated Control of Individual Magnetic Helical Microswimmers in a Swarm. *ACS Nano* **2018**, *12*, 6210−6217.

(7) Cheng, R.; Huang, W.; Huang, L.; Yang, B.; Mao, L.; Jin, K.; ZhuGe, Q.; Zhao, Y. Acceleration of Tissue Plasminogen Activator-Mediated Thrombolysis by Magnetically Powered Nanomotors. *ACS Nano* **2014**, *8*, 7746−7754.

(8) Tasci, T. O.; Disharoon, D.; Schoeman, R. M.; Rana, K.; Herson, P. S.; Marr, D. W. M.; Neeves, K. B. Enhanced Fibrinolysis with Magnetically Powered Colloidal Microwheels. *Small* **2017**, *13*, 1700954.

(9) Hu, J.; Huang, S.; Zhu, L.; Huang, W.; Zhao, Y.; Jin, K.; ZhuGe, Q. Tissue Plasminogen Activator-Porous Magnetic Microrods for Targeted Thrombolytic Therapy after Ischemic Stroke. *ACS Appl. Mater. Interfaces* **2018**, *10*, 32988−32997.

(10) Vilela, D.; Parmar, J.; Zeng, Y.; Zhao, Y.; Sánchez, S. Graphene-Based Microbots for Toxic Heavy Metal Removal and Recovery from Water. *Nano Lett.* **2016**, *16*, 2860−2866.

(11) Man, Y.; Lauga, E. The Wobbling-to-Swimming Transition of Rotated Helices. *Phys. Fluids* **2013**, *25*, 071904.
(12) Morozov, K. I.; Leshansky, A. M. The Chiral Magnetic Nanomotors. *Nanoscale* **2014**, *6*, 1580−1588.
(13) Tottori, S.; Zhang, L.; Qiu, F.; Krawczyk, K. K.; Franco-Obregón, A.; Nelson, B. J. Magnetic Helical Micromachines: Fabrication, Controlled Swimming, and Cargo Transport. *Adv. Mater.* **2012**, *24*, 811−816.
(14) Xin, C.; Yang, L.; Li, J.; Hu, Y.; Qian, D.; Fan, S.; Hu, K.; Cai, Z.; Wu, H.; Wang, D.; Wu, D.; Chu, J. Conical Hollow Microhelices with Superior Swimming Capabilities for Targeted Cargo Delivery. *Adv. Mater.* **2019**, *31*, 1808226.
(15) Abbott, J. J.; Peyer, K. E.; Lagomarsino, M. C.; Zhang, L.; Dong, L.; Kaliakatsos, I. K.; Nelson, B. J. How Should Microrobots Swim? *Int. J. Microbiol. Res.* **2009**, *28*, 1434−1447.
(16) Li, T.; Li, J.; Zhang, H.; Chang, X.; Song, W.; Hu, Y.; Shao, G.; Sandraz, E.; Zhang, G.; Li, L.; Wang, J. Magnetically Propelled Fish-Like Nanoswimmers. *Small* **2016**, *12*, 6098−6105.
(17) Jang, B.; Gutman, E.; Stucki, N.; Seitz, B. F.; Wendel-García, P. D.; Newton, T.; Pokki, J.; Ergeneman, O.; Pané, S.; Or, Y.; Nelson, B. J. Undulatory Locomotion of Magnetic Multilink Nanoswimmers. *Nano Lett.* **2015**, *15*, 4829−4833.
(18) Dreyfus, R.; Baudry, J.; Roper, M. L.; Fermigier, M.; Stone, H. A.; Bibette, J. Microscopic Artificial Swimmers. *Nature* **2005**, *437*, 862−865.
(19) Xie, H.; Sun, M.; Fan, X.; Lin, Z.; Chen, W.; Wang, L.; Dong, L.; He, Q. Reconfigurable Magnetic Microrobot Swarm: Multimode Transformation, Locomotion, and Manipulation. *Sci. Rob.* **2019**, *4*, No. eaav8006.
(20) Li, T.; Zhang, A.; Shao, G.; Wei, M.; Guo, B.; Zhang, G.; Li, L.; Wang, W. Janus Microdimer Surface Walkers Propelled by Oscillating Magnetic Fields. *Adv. Funct. Mater.* **2018**, *28*, 1706066.
(21) Li, Z.; Yang, F.; Yin, Y. Smart Materials by Nanoscale Magnetic Assembly. *Adv. Funct. Mater.* **2020**, *30*, 1903467.
(22) Liao, P.; Xing, L.; Zhang, S.; Sun, D. Magnetically Driven Undulatory Microswimmers Integrating Multiple Rigid Segments. *Small* **2019**, *15*, 1901197.
(23) Helgesen, G. Magnetic Propulsion of Microspheres at Liquid-Glass Interfaces. *J. Appl. Phys.* **2018**, *123*, 064902.
(24) Mair, L. O.; Evans, B. A.; Nacev, A.; Stepanov, P. Y.; Hilaman, R.; Chowdhury, S.; Jafari, S.; Wang, W.; Shapiro, B.; Weinberg, I. N. Magnetic Microkayaks: Propulsion of Microrods Precessing near a Surface by Kilohertz Frequency, Rotating Magnetic Fields. *Nanoscale* **2017**, *9*, 3375−3381.
(25) Sing, C. E.; Schmid, L.; Schneider, M. F.; Franke, T.; Alexander-Katz, A. Controlled Surface-Induced Flows from the Motion of Self-assembled Colloidal Walkers. *Proc. Natl. Acad. Sci. U.S.A.* **2010**, *107*, 535.
(26) Xie, M.; Zhang, W.; Fan, C.; Wu, C.; Feng, Q.; Wu, J.; Li, Y.; Gao, R.; Li, Z.; Wang, Q.; Cheng, Y.; He, B. Bioinspired Soft Microrobots with Precise Magneto-Collective Control for Micro-vascular Thrombolysis. *Adv. Mater.* **2020**, *32*, 2000366.
(27) Huang, W.; Yang, F.; Zhu, L.; Qiao, R.; Zhao, Y. Manipulation of Magnetic Nanorod Clusters in Liquid by Non-uniform Alternating Magnetic Fields. *Soft Matter* **2017**, *13*, 3750−3759.
(28) Yang, L.; Yu, E.; Vong, C.-I.; Zhang, L. Discrete-Time Optimal Control of Electromagnetic Coil Systems for Generation of Dynamic Magnetic Fields with High Accuracy. *IEEE ASME Trans. Mechatron.* **2019**, *24*, 1208.
(29) Jang, B.; Hong, A.; Alcantara, C.; Chatzipirpiridis, G.; Martí, X.; Pellicer, E.; Sort, J.; Harduf, Y.; Or, Y.; Nelson, B. J.; Pané, S. Programmable Locomotion Mechanisms of Nanowires with Semihard Magnetic Properties near a Surface Boundary. *ACS Appl. Mater. Interfaces* **2018**, *11*, 3214−3223.
(30) Bonilla-Brunner, A.; Llorente García, I.; Jang, B.; Amano Patiño, M.; Alimchandani, V.; Nelson, B. J.; Pané, S.; Contera, S. Polymeric Microellipsoids with Programmed Magnetic Anisotropy for Controlled Rotation using Low (≈ 10 mT) Magnetic Fields. *Appl. Mater. Today* **2020**, *18*, 100511.
(31) Zhou, Q.; Petit, T.; Choi, H.; Nelson, B. J.; Zhang, L. Dumbbell Fluidic Tweezers for Dynamical Trapping and Selective Transport of Microobjects. *Adv. Funct. Mater.* **2017**, *27*, 1604571.
(32) Zhang, Y.; Zhang, L.; Yang, L.; Vong, C. I.; Chan, K. F.; Wu, W. K. K.; Kwong, T. N. Y.; Lo, N. W. S.; Ip, M.; Wong, S. H.; Sung, J. J. Y.; Chiu, P. W. Y.; Zhang, L. Real-time Tracking of Fluorescent Magnetic Spore−based Microrobots for Remote Detection of C. diff Toxins. *Sci. Adv.* **2019**, *5*, No. eaau9650.
(33) Gao, W.; Sattayasamitsathit, S.; Wang, J. Catalytically Propelled Micro-/nanomotors: How Fast can they Move? *Chem. Rec.* **2012**, *12*, 224−231.
(34) Rashidi, M. M.; Johnson, S.; Yang, Z. Theoretical Study of Moving Magnetic Beads on an Inclined Plane and its Application in the Ratchet Separation Technique. *J. Magn. Magn. Mater.* **2016**, *398*, 13−19.
(35) Sugimoto, T.; Khan, M. M.; Muramatsu, A.; Itoh, H. Formation Mechanism of Monodisperse Peanut-type α-Fe_2O_3 Particles from Condensed Ferric Hydroxide Gel. *Colloids Surf., A* **1993**, *79*, 233−247.
(36) Cao, H.; Wang, G.; Zhang, L.; Liang, Y.; Zhang, S.; Zhang, X. Shape and Magnetic Properties of Single-crystalline Hematite (α-Fe_2O_3Nanocrystals. *ChemPhysChem* **2006**, *7*, 1897−1901.
(37) Hill, A. H.; Jiao, F.; Bruce, P. G.; Harrison, A.; Kockelmann, W.; Ritter, C. Neutron Diffraction Study of Mesoporous and Bulk Hematite, α-Fe_2O_3. *Chem. Mater.* **2008**, *20*, 4891−4899.
(38) Geng, F.; Cong, H. Fe-filled Carbon Nanotube Array with High Coercivity. *Physica B* **2006**, *382*, 300−304.
(39) Chevalier, A.; Le Floc'h, M. Dynamic Permeability in Soft Magnetic Composite Materials. *J. Appl. Phys.* **2001**, *90*, 3462−3465.
(40) Lee, S. H.; Liddell, C. M. Anisotropic Magnetic Colloids: a Strategy to Form Complex Structures using Nonspherical Building Blocks. *Small* **2009**, *5*, 1957−1962.
(41) Krahne, R.; Manna, L.; Morello, G.; Figuerola, A.; George, C.; Deka, S. *Physical Properties of Nanorods*; Springer: Berlin, Heidelberg, Germany, 2013.
(42) Ghosh, A.; Mandal, P.; Karmakar, S.; Ghosh, A. Analytical Theory and Stability Analysis of an Elongated Nanoscale Object under External Torque. *Phys. Chem. Chem. Phys.* **2013**, *15*, 10817−10823.
(43) Happel, J.; Brenner, H. *Low Reynolds Number Hydrodynamics: With Special Applications to Particulate Media*; Springer Science & Business Media: Berlin, Germany, 2012.
(44) Zhang, F.; Zhuang, J.; Esteban Fernández de Ávila, B.; Tang, S.; Zhang, Q.; Fang, R. H.; Zhang, L.; Wang, J. A Nanomotor-Based Active Delivery System for Intracellular Oxygen Transport. *ACS Nano* **2019**, *13*, 11996−12005.
(45) Chwang, A. T.; Wu, T. Y.-T. Hydromechanics of low-Reynolds-number flow. Part 2. Singularity method for Stokes flows. *J. Fluid Mech.* **1975**, *67*, 787−815.
(46) Yang, S.-M.; Leal, L. G. Particle Motion in Stokes Flow near a Plane Fluid-Fluid Interface. Part 1. Slender Body in a Quiescent Fluid. *J. Fluid Mech.* **1983**, *136*, 393−421.
(47) Mahoney, A. W.; Nelson, N. D.; Peyer, K. E.; Nelson, B. J.; Abbott, J. J. Behavior of Rotating Magnetic Microrobots above the Step-out Frequency with Application to Control of Multi-microrobot Systems. *Appl. Phys. Lett.* **2014**, *104*, 144101.
(48) Xie, H.; Fan, X.; Sun, M.; Lin, Z.; He, Q.; Sun, L. Programmable Generation and Motion Control of a Snakelike Magnetic Microrobot Swarm. *IEEE ASME Trans. Mechatron.* **2019**, *24*, 902−912.
(49) Lee, E.; Huang, D.; Luo, T. Ballistic Supercavitating Nanoparticles Driven by Single Gaussian Beam Optical Pushing and Pulling Forces. *Nat. Commun.* **2020**, *11*, 2404.
(50) Tottori, S.; Zhang, L.; Qiu, F.; Krawczyk, K. K.; Franco-Obregón, A.; Nelson, B. J. Magnetic Helical Micromachines: Fabrication, Controlled Swimming, and Cargo Transport. *Adv. Mater.* **2012**, *24*, 811−816.

https://dx.doi.org/10.1021/acs.langmuir.0c02132
Langmuir 2020, 36, 11125−11137